MATERIALS CHEMISTRY
FRONTIERS

CCS 中国化学会 CHINESE CHEMICAL SOCIETY
ICCAS
ROYAL SOCIETY OF CHEMISTRY

RESEARCH ARTICLE

View Article Online
View Journal | View Issue

Cite this: *Mater. Chem. Front.*, 2026, **10**, 491

Mechanically rigid 2D lead halide perovskite $(PMA)_2PbCl_4$ with pressure-stable broadband emission

Muhammad Azeem, [a] Jinhyuk Choi, [b] Yeonhak Jung [a] and Yongjae Lee *[a]

Received 3rd October 2025,
Accepted 3rd December 2025

DOI: 10.1039/d5qm00719d

rsc.li/frontiers-materials

We present a combined experimental and theoretical investigation of the pressure response of the chlorine-based two-dimensional perovskite $(PMA)_2PbCl_4$. High-pressure synchrotron powder X-ray diffraction (HP-PXRD), photoluminescence spectroscopy (HP-PL), and density functional theory (DFT) calculations reveal that compression up to 5.45 GPa induces pronounced anisotropic lattice contraction and partial amorphization, while decompression reveals phase reversibility. The $PbCl_6$ octahedra remain mechanically rigid, with distortions accommodated by octahedral tilts, flattening, and migration of phenylmethylammonium cations (PMA^+), leading to interlayer planarization and enhanced electron–phonon coupling. Elastic tensor analysis confirms moderate mechanical anisotropy and coexisting auxetic and conventional elastic responses. HP-PL demonstrates a pressure-driven crossover between narrow free-exciton emission (quenched by 1.84 GPa) and more resilient broadband self-trapped exciton emission (persisting up to 7.8 GPa with its maximum intensity at ~4.5 GPa). Overall, the compression-driven structure–property evolution maintains broadband emission, which leads to increased nonradiative losses at higher pressures. The combined results establish $(PMA)_2PbCl_4$ as a mechanically robust, pressure-tunable broadband emitter with strong potential for stable optoelectronic applications.

Introduction

Two-dimensional (2D) hybrid organic–inorganic perovskites (HOIPs) have emerged as versatile functional materials due to their unique structural flexibility, environmental robustness, and tunable optoelectronic properties.[1–4] Amongst them, the layered Ruddlesden–Popper -type structure, when composed of corner-sharing PbX_6 octahedral sheets separated by organic cations, forms natural quantum wells that enhance exciton confinement and photoluminescence efficiency while simultaneously imparting superior moisture tolerance compared to its three-dimensional counterparts.[5,6] These attributes have positioned 2D HOIPs as promising candidates for photovoltaics, light-emitting diodes (LEDs), photodetectors, lasing, and scintillation devices.[7–9] A particularly compelling feature of 2D HOIPs is their ability to exhibit broadband emission (BBE) from self-trapped excitons (STEs), which can be exploited for low-cost, single-component, white-light sources.[10,11] Unlike conventional multiphosphor strategies, STE-driven emission arises from lattice distortions and strong electron–phonon coupling, providing a robust pathway for white-light generation.[12–14] In this context, structural distortions of Pb–X octahedra, either intrinsic or externally induced, play a pivotal role in stabilizing STEs and enhancing radiative yield.[15] Pressure has emerged as a powerful and chemically clean thermodynamic parameter to tune the structural and optoelectronic properties of halide perovskites.[16] By altering lattice dimensions, octahedral tilting, and interlayer coupling, compression can suppress free-exciton emission (FEE) while activating broadband STE emission, thereby inducing emissive states inaccessible under ambient conditions.[16–18] While extensive pressure-induced phenomena such as phase transitions, amorphization, and symmetry breaking have been documented in 3D perovskites, systematic studies of pressure effects in 2D HOIPs remain comparatively limited despite their greater structural diversity and excitonic tunability. Chlorine-based 2D perovskites, in particular, offer stronger Pb–Cl bonding and additional noncovalent interactions compared to their iodide or bromide analogues[8] suggesting enhanced mechanical rigidity and distinctive excitonic responses under pressure.[19] Yet, their high-pressure structure–property relationships remain underexplored.

Here, we report a comprehensive high-pressure study of the chlorine-based 2D perovskite $(PMA)_2PbCl_4$, integrating synchrotron powder X-ray diffraction, photoluminescence spectroscopy, and density functional theory calculations. By correlating anisotropic lattice compression, octahedral tilting

[a] *Department of Earth System Sciences, Yonsei University, 50 Yonsei-ro, Seodaemun-gu, Seoul 03722, Republic of Korea. E-mail: yongjaelee@yonsei.ac.kr*
[b] *Pohang Accelerator Laboratory, POSTECH, Pohang 37673, Republic of Korea*

and flattening, and organic–inorganic coupling with excitonic behavior, we reveal how pressure governs the crossover between free-exciton and broadband self-trapped exciton emission. Our findings not only uncover the structural and elastic origins of mechanical rigidity and emission resilience in $(PMA)_2PbCl_4$ but also establish a coherent structure–property pathway that links compression-driven lattice distortions to pressure-tunable luminescence. This work further provides critical insights into designing mechanically stable, broadband-emissive halide perovskites for next-generation optoelectronic applications.

Results and discussion

$(PMA)_2PbCl_4$ crystallizes in the orthorhombic space group $Cmc2_1$ under ambient conditions, with unit cell parameters of a = 33.4497(2) Å, b = 7.8376(1) Å, and c = 7.7501(1) Å, and a cell volume of 2031.80(3) Å^3. The structure consists of terminal $(PbCl_4)^{2-}$ layers separated by bilayers of benzylamine or phenylmethylammonium (PMA^+) cations.[19] These organic cations cap the inorganic sheets on both sides, resulting in a quasi-two-dimensional monolayer with a thickness of ~1.75 nm. Adjacent monolayers are held together by weak van der Waals forces along the crystallographic a-axis, as illustrated in Fig. S1 (SI). The phase purity under ambient conditions is illustrated in Fig. S2, exhibiting good agreement with the reported data.[8] In contrast, the iodide analogue HOIP $(PMA)_2PbI_4$ crystallizes in the orthorhombic *Pbca* space group, with a thinner monolayer (~1.44 nm) yet a larger unit cell volume (V = 2301.5(5) Å^3).[3] High-pressure powder X-ray diffraction (HP-PXRD) reveals that $(PMA)_2PbCl_4$ remains stable up to 5.45 (± 0.4) GPa, with a systematic shift of diffraction peaks to higher angles accompanied by gradual peak broadening (Fig. 1a). Unlike the iodide counterpart, which undergoes a phase transition near 1.12 GPa,[3] the chloride phase persists, in part, attributable to stronger Pb–Cl and Cl–Cl bonding and additional noncovalent interactions. The observed peak broadening and intensity loss by ~5.45 GPa indicate the onset of partial amorphization, though less pronounced compared with the iodide analogue, consistent with the intrinsic softness of the HOIP frameworks.[3,20] Pressure-dependent unit cell volume and axis lengths were driven using Le-Bail whole-profile fitting,[21] which were then subjected to fitting to a third-order Birch–Murnaghan equation of state (BM-EOS) (eqn (1))[22] using EosFit7-GUI[23] (Fig. 1b and Fig. S3), to quantify pronounced anisotropic compression behaviors, *i.e.*, the a-, b-, and c-axes contract by ~13.4%, ~4.8%, and ~3.8%, respectively, corresponding to linear compressibilities of ~24.85, ~8.49, and ~6.79 TPa^{-1} (eqn (1)):

$$P = \frac{3}{2}K_{T_0}\left[\left(\frac{V_0}{V}\right)^{\frac{7}{3}} - \left(\frac{V_0}{V}\right)^{\frac{5}{3}}\right] \times \left\{1 + \frac{3}{4}\left(K'_{T_0} - 4\right)\left[\left(\frac{V_0}{V}\right)^{\frac{2}{3}} - 1\right]\right\} \quad (1)$$

While the unit cell volume decreases by ~20.7% over the entire pressure range, leading to a volumetric compressibility of 37.25 TPa^{-1}, the linear compressibilities (Fig. S4) calculated using a freely available webtool (PASCal) for Principal Axis Strain Calculations,[24] highlight strong directional rigidity, with compression dominated by collapse along the a-axis, where van der Waals gaps accommodate structural densification. The resulting bulk modulus of $(PMA)_2PbCl_4$, K_0 = 15.31 (± 1.3) GPa, falls within the 7-28 GPa range typical of 2D HOIPs but surpasses that of its iodide analogue (11.4–14.8 GPa),[3] reflecting stronger Pb–Cl and Cl–Cl bonding reinforced by Cl···H interactions.[8] Compressibility anisotropy analysis (Fig. S4) reveals that the inorganic framework dominates lattice rigidity,

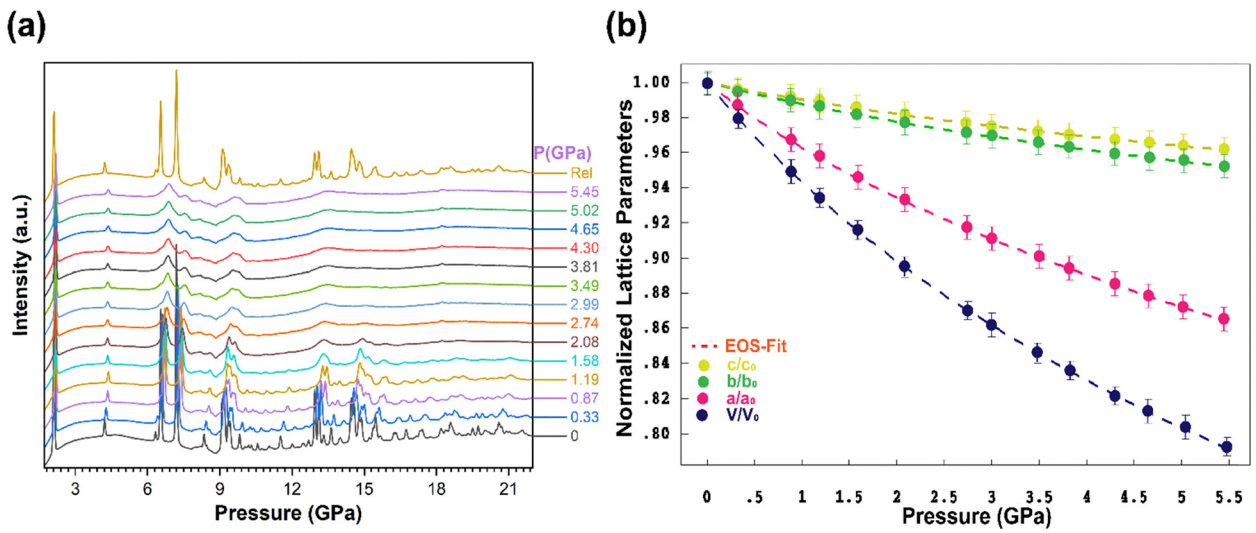

Fig. 1 High-pressure structural evolution of $(PMA)_2PbCl_4$. (a) *In situ* synchrotron PXRD patterns collected upon compression up to 5.45 (± 0.4) GPa. (b) Fitting the normalized lattice parameters and volume through third-order BM-EOS using EosFit7-GUI.

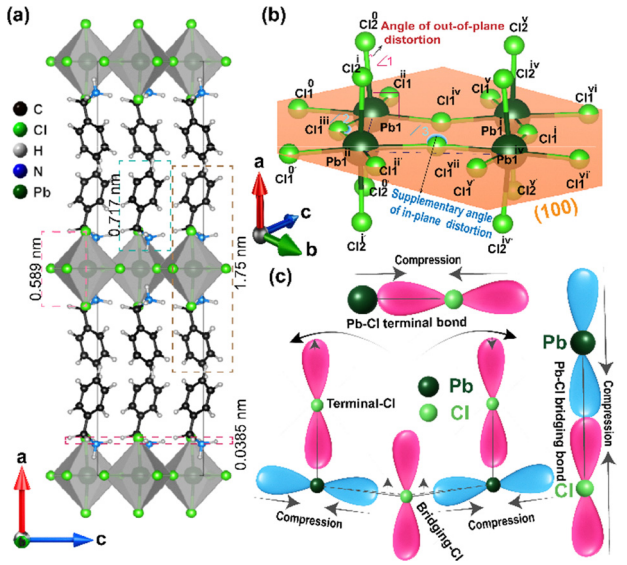

Fig. 2 High-pressure evolution of the $(PMA)_2PbCl_4$ crystal structure derived using DFT calculations. (a) The layered structure viewed along the *b*-axis. (b) In-plane and out-of-plane distortions by bridging and terminal Cl atoms. (c) Schematic diagrams of Pb–Cl bonds and Pb–Cl–Pb angle configurations.

while the organic spacer layer accommodates deformation.[25] The *c*-axis exhibits a greater stiffness due to the uninterrupted corner-sharing PbI_6 octahedral layer, whereas the *b*-axis exhibits comparable stiffness with enhanced Young's modulus as strong Pb–Cl bonding concentrates electron density. Such directional compression hierarchy, *i.e.*, the most rigid *c*-axis, the moderately stiff *b*-axis, and the most compressible *a*-axis, highlights the cooperative role of inorganic connectivity and organic flexibility in governing the overall anisotropic mechanical response, consistent with the theoretical predictions outlined below. Given the structural complexity and a large asymmetric unit, Rietveld refinement was deemed impractical;[26] therefore, DFT calculations were employed using experimentally determined lattice parameters at selected pressures.[3,26] The optimized structures at 0, 2.74, and 4.30 GPa reveal a systematic reduction in interlayer spacing, with the corresponding layer thicknesses decreasing from ~1.75 nm to ~1.48 nm. These structural models are presented in Fig. 2a and Fig. S1, confirming the progressive densification, which highlights the collapse of the layered perovskite structure under compression. Notably, $(PMA)_2PbCl_4$ exhibits only ~1.54% reduction in the monolayer thickness, compared with ~3.5% reduction for $(PMA)_2PbI_4$ over a similar pressure range,[3] indicating that the Cl-based HOIP is significantly less compressible. DFT analysis of the representative octahedral cluster reveals progressive flattening under compression to 4.30 GPa: selected ∠Pb–Cl–Pb bridging angles, *e.g.*, centers $Pb1–Pb1^{i}$ and bridges $Cl1^{i}–Cl1^{iv}$, increase by up to ~2.2%, while inter-octahedral Pb–Pb separation shrinks by 3–4%, reflecting anisotropic compression along the *b*- and *c*-axes compared to the *a*-axis (Fig. S5 and S6). In contrast, the ∠Cl–Pb–Cl bond angles involving bridging chlorine atoms exhibit a consistent trend of either slight expansion (ranging from 0.4% to 1.0%) or notable contraction (up to 1.7%). However, the ∠Cl–Pb–Cl angles formed between bridging and terminal chlorine atoms demonstrate modulated overall variation, with approximately 75% of these angles contracting by less than ~1%, while the remaining 25% show an increase of ~0.93% (Table S2). These collective changes drive the cooperative tilt along the *a*-axis and rotations about the *b*- and *c*-axes (Fig. 3 and Fig. S5–S8). Importantly, the tilting responses of the symmetry-related octahedra mirror each other, producing alternating increases and decreases in tilt rather than unidirectional rotations. Such distortions arise from the anisotropic compressibility of the lattice and are further modulated by interactions with the organic cations displaced toward the inorganic sheet (Fig. S9). Moreover, the in-plane and out-of-plane distortions contributing to the overall distortion of the octahedral layer are characterized by the in-plane angles (∠Pb–X–Pb) and by the shift of the axial Pb–X bonds from the normal to the plane of

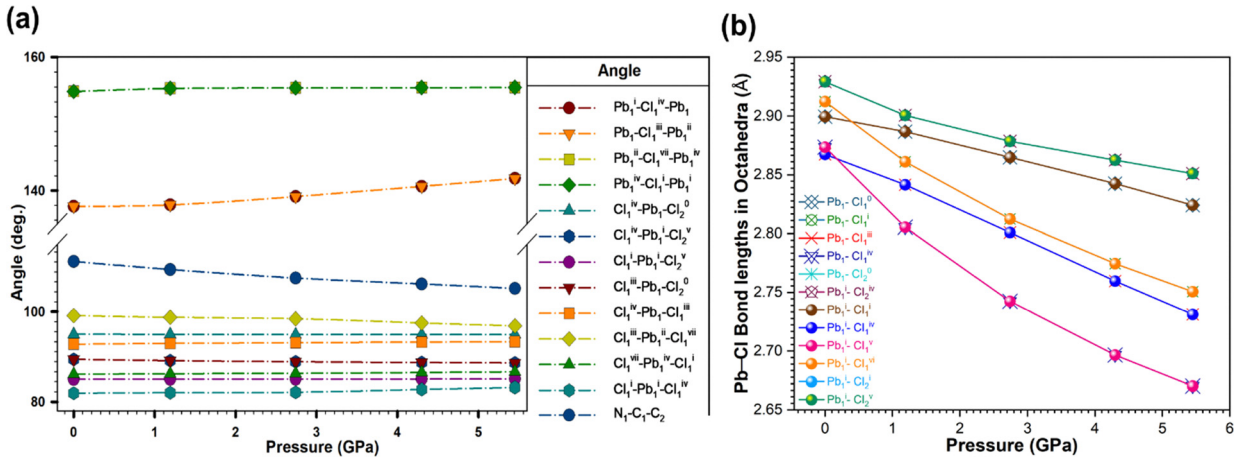

Fig. 3 Pressure-dependent structural evolution of $(PMA)_2PbCl_4$: (a) variations of bridging bond angles centered at Cl atoms, Pb-centered angles between terminal and bridging Cl atoms, and ∠N–C–C. (b) Pressure-induced changes in Pb–Cl bond lengths within two adjacent octahedra.

Pb atoms, respectively.[8] Similarly, the octahedral tilting in $(PMA)_2PbCl_4$ exhibits both in-plane and out-of-plane distortions. Specifically, the Pb1- and $Pb1^i$-centered octahedra tilt out-of-plane along the [011] direction and exhibit in-plane distortions along the [100][8] direction. The out-of-plane distortion is characterized by angle ∠1, while the in-plane distortion is represented by angles ∠2 and ∠3. These in-plane angles are supplementary and can be defined as ∠2 + ∠Pb1–Cl^{iii}–$Pb1^{ii}$ = 180° and ∠3 + ∠$Pb1^{iv}$–Cl^{iii}–$Pb1^{ii}$ = 180°. The distortion angles decreased by ∼1.4%, ∼7.1%, and ∼2.3%, respectively (Fig. 2b and Fig. S7 and Table S2). Concurrently, equatorial Pb–Cl bonds contract significantly over 0–4.30 GPa compression, with reductions ranging from ∼2.3% to ∼6.2% (Fig. S8 and Table S2), confirming anisotropic mechanical behavior governed by rigid Pb–Cl bonding and intermolecular interactions within the inorganic sheets (Fig. 3).[8] Beyond octahedral distortions, the PMA^+ spacer cations undergo marked pressure-driven reconfiguration, *e.g.*, the C–C distances shorten by 0.5–1.9%, while the ∠N–C–C angle decreases by 4.6%, indicating bending of the benzene ring toward the nitrogen and opposing motions of the carbon subgroups (Fig. S10 and S11). Terminal N–Pb distances contract by ∼6.3–8.6%, evidencing inward migration of the organic cation into the inorganic framework (Fig. S12 and Table S2). This cooperative motion, combined with octahedral tilting, drives pronounced collapse along the *a*-axis, where the rigid Pb–Cl bonds align parallel to cation displacement. The asymmetric interplay of inorganic rigidity and organic flexibility highlights the critical role of host–guest interactions in dictating the observed high-pressure structural evolution.

To quantify this behavior, the second-order elastic tensor was computed at 0 GPa *via* DFT. The derived bulk modulus agrees with the experimental values (Table 1), and all elastic stability criteria for orthorhombic systems are satisfied, confirming the mechanical robustness of $(PMA)_2PbCl_4$ under compression.[31]

$$C_{11} > 0, C_{22} > 0, C_{33} > 0, C_{44} > 0, \quad (2)$$

$$C_{55} > 0, C_{66} > 0, C_{22} + C_{33} - 2C_{23} > 0, \quad (3)$$

$$C_{11} + C_{22} - 2C_{12} > 0, C_{11} + C_{33} - 2C_{13} > 0, \quad (4)$$

$$C_{11} + C_{22} + C_{33} + 2(C_{12} + C_{13} + C_{23}) > 0 \quad (5)$$

The bulk modulus derived from the elastic tensor, 13.22 (± 2.6) GPa, is in close agreement with the HP-PXRD-derived value of 15.31 (± 1.3) GPa, validating the computational approach. Furthermore, the elastic property maps (Fig. 4) confirm pronounced anisotropy, *e.g.*, Young's modulus (*E*) reaches 26.1 GPa along ⟨011⟩ but falls to 8.5 GPa along ⟨010⟩, yielding an anisotropy ratio (A_E) of ∼3.1, approximately 1.6 times lower than that of its bromide analogue. The shear modulus spans 3.8–9.5 GPa, giving A_G = 2.5, about half the value reported for $(BA)_2PbBr_4$.[20] On the other hand, Poisson's ratio is distributed over 0.11–0.60, reflecting both brittle and anisotropic responses under strain (Fig. S13–S15).[32,33] Velocity surface plots (Fig. 4d and Fig. S15) further illustrate the anisotropic character, *i.e.*, longitudinal velocity is the lowest along [100], consistent with the highest compressibility of the *a*-axis, and highest along [001], where the most stiff *c*-axis resists deformation. The complementary slowness surfaces ($s = 1/v$) emphasize the observed axial contrast, bulging along the compliant *a*-axis and contracting along the rigid *c*-axis (Fig. S13 and S15).[34]

Collectively, these results demonstrate that elastic rigidity and acoustic propagation in $(PMA)_2PbCl_4$ are strongly directional, with maximum softness aligned to the most compressible axis and robustness retained along the least compressible direction. *In situ* high-pressure photoluminescence (HP-PL) measurements reveal a pressure-induced crossover in $(PMA)_2PbCl_4$ from narrow free-exciton emission (FEE) to broadband self-trapped exciton (BBE) emission (Fig. 5a). FEE redshifts are fully quenched at ∼1.84 GPa, whereas BBE persists up to ∼7.8 GPa, peaking in intensity near 4.5 GPa (Fig. 5c). The anti-correlated intensity and FWHM trends confirm enhanced self-trapping at moderate pressures (<1.84 GPa) followed by nonradiative losses at higher pressures (>4.48 GPa). The driving force is attributed to the pronounced anisotropic lattice

Table 1 Comparison of reported bulk moduli for two-dimensional hybrid organic–inorganic perovskites from various studies, distinguished by the material compositions and measurement methods

Formula	Organic cation	Method	Bulk-mod. (GPa)	Ref.
$(BTa)_2PbI_4$	$I_4C_{16}H_{22}N_9^+$	3rd-BM-EOS	10.3	27
$(F_2BTa)_2PbI_4$	$F_4I_4C_{16}H_{18}N_9^+$	3rd-BM-EOS	12.3	27
$(BA)_2PbI_4$	$C_6H_5CH_2NH_3^+$	3rd-BM-EOS	11.4	3
$(ClPMA)_2PbI_4$	$ClC_6H_4CH_2NH_3^+$	3rd-BM-EOS	16.8	26
$(BA)_2PbBr_4$	$C_6H_5CH_2NH_3^+$	2nd-BM-EOS	10.0	20
$(PEA)_2PbI_4$	$C_6H_5C_2H_4NH_3^+$	DFT	12.0	28
$(FPEA)_2PbI_4$	$FC_6H_4C_2H_4NH_3^+$	DFT	13.6	28
$(BA)_2PbI_4$	$CH_3(CH_2)_3NH_3^+$	DFT	11.5	28
$(BZA)_2PbI_4$	$C_6H_5CH_2NH_3^+$	DFT	12.7	28
$(PEA)_2PbCl_4$	$C_6H_5C_2H_4NH_3^+$	DFT	14.1	28
$(ClPMA)_2PbI_4$	$ClC_6H_4CH_2NH_3^+$	DFT	15.0	26
$(C_6H_5CH_2NH_3)_2PbI_4$	$C_6H_5CH_2NH_3^+$	DFT	11.9	19
$(BA)_2PbI_4$	$CH_3(CH_2)_3NH_3^+$	DFT	6.4	19
$(BA)_2PbI_4$	$CH_3(CH_2)_3NH_3^+$	DFT	7.3	29
$(5\text{-}AVA)_2PbI_4$	$HOOC(CH_2)_4NH_3^+$	DFT	8.1	30
$(C_6H_5CH_2NH_3)_2PbCl_4$	$C_6H_5CH_2NH_3^+$	Nano-indentation	10.5	19
$(PMA)_2PbCl_4$	$C_6H_5CH_2NH_3^+$	3rd-BM-EOS	15.3 (± 1.3)	This work
$(PMA)_2PbCl_4$	$C_6H_5CH_2NH_3^+$	DFT	13.2 (± 2.6)	

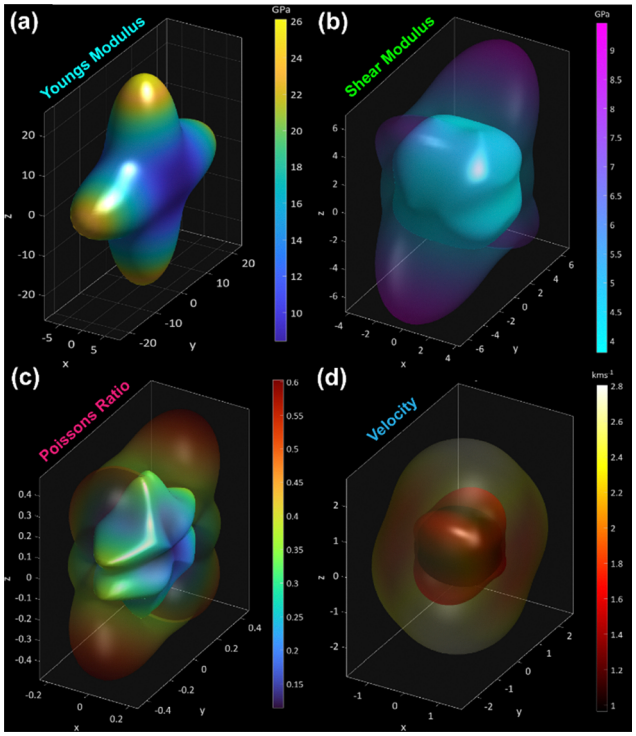

Fig. 4 Three-dimensional anisotropy maps of the mechanical properties of $(PMA)_2PbCl_4$. (a) Young's modulus E. (b) Shear modulus G. (c) Poisson's ratio ν. (d) Sound velocity v. In (b)–(d), the translucent outer shell denotes the maximum values, with the opaque inner shell denoting the minimum values.

compression, *i.e.*, $a/a_0 = 13.4\% \gg b/b_0 = 4.8\% > c/c_0 = 3.8\%$, and volume collapse near 5.45 GPa, which stiffens the *c*-axis and softens the *a*-axis. The DFT models then show progressive interlayer planarization (thickness reduction from 1.75 to 1.48 nm from ambient to 4.30 GPa), octahedral flattening and tilting, and shorter Pb–Cl bonds—distortions that enhance electron–phonon coupling and stabilize self-trapped excitons. Elastic and acoustic maps corroborate this anisotropy, showing suppressed longitudinal velocity along the compliant *a*-axis and the fastest propagation along the rigid *c*-axis, conditions favorable for polaron localization within the inorganic layers.[35] The rapid quenching of FEE is thus attributed to pressure-driven self-trapping of excitons and activation of nonradiative pathways, while the persistence of BBE arises from radiative recombination of stabilized STE states.[36] Above ~4.5 GPa, further densification promotes multiphonon relaxation and defect formation (evidenced by PXRD amorphization), narrowing the emission window and reducing intensity.[37] Control measurements, including ruby-calibrated pressures, silicone-oil PTM, and reversibility checks,[38] confirm the intrinsic origin of the observed behavior without significant chemical degradation. This FE to STE emissive reconfiguration mirrors previous reports on other 2D HOIPs, where low dimensionality and octahedral distortions enhance exciton binding and broadband emission under hydrostatic stress.[39] Comparable pressure-activated BBE plateaus followed by quenching in bromide and iodide analogues support the same distortion-assisted self-trapping mechanism. Overall, Fig. 5 encapsulates the coherent structure–property pathway: anisotropic compression

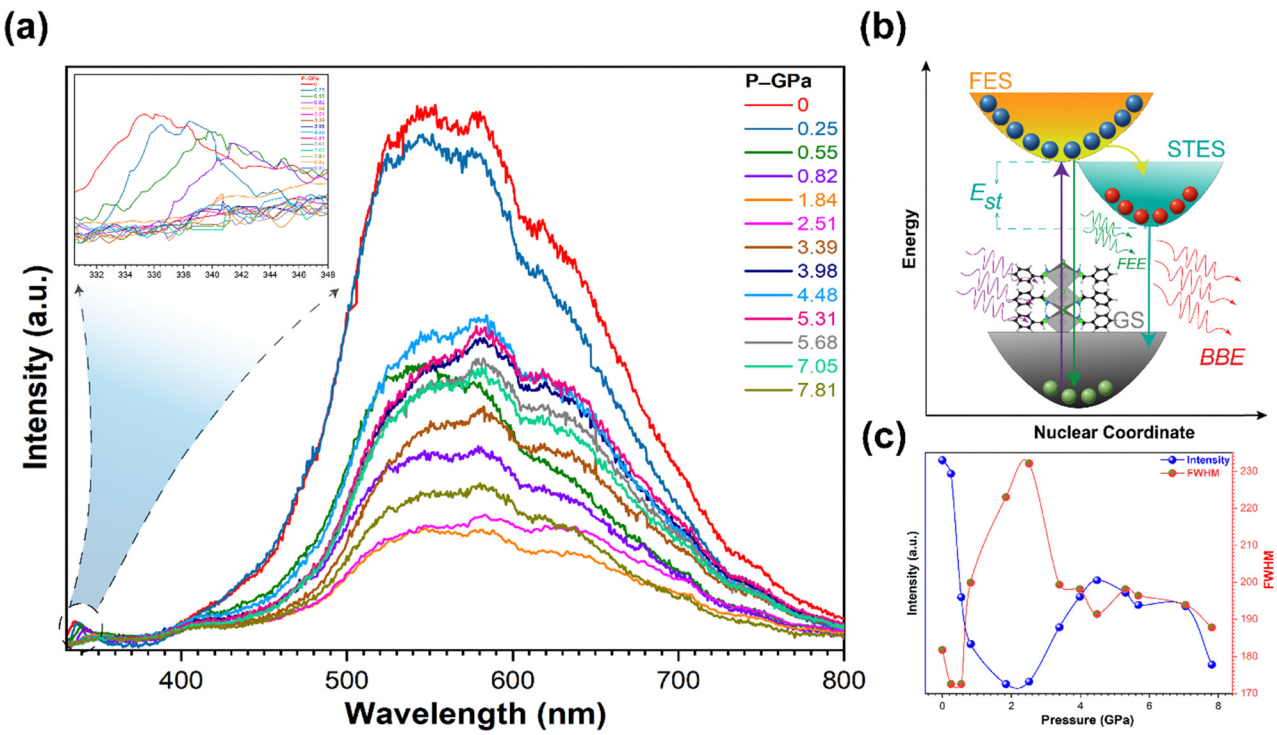

Fig. 5 Pressure-dependent photoluminescence behavior of $(PMA)_2PbCl_4$. (a) PL spectra obtained from ambient to 7.81 GPa, with the inset depicting the evolution of FEE. (b) Schematic diagram of FEE and BBE due to free excitons and self-trapped excitons. (c) Intensity and FWHM under compression.

drives octahedral tilting, layer flattening, and interlayer coupling, strengthening electron–phonon interactions, suppressing FEE, enabling BBE dominance, and ultimately leading to nonradiative loss at higher pressures. Furthermore, the PL spectrum of the recovered sample matches that observed under ambient conditions prior to compression, indicating the structural reversibility of $(PMA)_2PbCl_4$ (Fig. S16). As a result, the CIE 1931 plot locates the chromaticity coordinates at (0.402, 0.467) (Fig. S17), which lie near the warm-white region (CCT = 4076 K) and slightly above the blackbody locus (Duv = 0.0316), consistent with the pressure-stabilized broadband STE emission in this 2D HOIP.[40] A moderate color-rendering index (CRI = 76) but low R9 ($\sim$1) reflects limited deep-red content despite a wide spectral envelope.[41] The corresponding SPD spans $\sim$450–800 nm with a plateau centered in the green–yellow ($\sim$520–620 nm) region and a long red tail, capturing the characteristic wide, featureless BBE band discussed above.[42]

Experimental

Synthesis

All chemicals and solvents were of reagent grade and were used as received without further purification. In a typical synthesis, lead chloride ($PbCl_2$) and phenylmethylammonium chloride (PMACl = $C_6H_5CH_2NH_3Cl$) were dissolved (1 : 2 molar ratio) in 5 mL of DMF in a glass vessel. Subsequently, $PbCl_2$-PMACl-DMF was mixed with continuous magnetic stirring for 24 hours at room temperature, and the solution was filtered to remove undissolved particles. The vessel was left undisturbed in a fume hood at room temperature for 72 hours. After this period, white, plate-like single crystals formed at the bottom of the vessel. These crystals were collected by filtration and washed with chilled diethyl ether to remove residual reactants.[43]

High-pressure synchrotron XRD

In situ HP-PXRD was performed using a diamond anvil cell (DAC) with a culet diameter of 500 μm and a stainless-steel gasket of 40 μm thickness. Synchrotron radiation (λ = 0.6884(1) Å) was focused on a 36 × 12 μm^2 spot through Kirkpatrick–Baez mirrors to collect data using a Pilatus 2 M detector, which was processed *via* the FIT2D suite of packages[44] at the 3D beamline at Pohang Light Source II (PLS-II) at Pohang Accelerator Laboratory (PAL).[45] A well-ground powder sample was loaded into a hole of the above-mentioned stainless-steel gasket (220 μm in diameter) with a few ruby balls. The ruby chips were used for pressure calibration, while silicone oil was added as a pressure-transmitting medium in the DAC. The pressure was determined by the ruby fluorescence method inside the DAC with an error of $\sim$0.1 GPa.[46,47] The unit cell parameters for different pressures were refined by the Le-Bail method using the GSAS-II program.[48]

High-pressure photoluminescence

The HP-PL spectra were recorded using a Raman spectrometer (Horiba, LabRam Aramis) equipped with a 325 nm He-Cd laser (3 mW) as the excitation source, operated in reflection mode at the Yonsei Center for Research Facilities at Yonsei University.[26] A long working distance 40× microscope objective focused the excitation beam onto the sample mounted inside the DAC. The emitted PL signal was dispersed using a 600 lines per mm diffraction grating (centered at 750 nm) and collected with a single accumulation, using an exposure time of 5 seconds. The applied pressure and its calibration were conducted following the same procedures as described in the aforementioned methods.[26]

First-principles calculations

First-principles calculations were carried out using the CASTEP code (CAmbridge Serial Total Energy Package),[49] a plane-wave pseudopotential total energy package based on DFT[50] to perform structural geometry optimizations. The Perdew–Burke–Ernzerhof (PBE) exchange–correlation functional within the generalized gradient approximation (GGA) was employed, along with on-the-fly generated (OTFG) ultrasoft pseudopotentials.[51] A plane-wave cutoff energy of 570 eV was used,[26] and Brillouin zone sampling was performed using a Monkhorst–Pack *k*-point grid of 2 × 2 × 1, corresponding to a *k*-point spacing finer than 0.04 $Å^{-1}$.[52] Geometry optimizations were conducted using the Broyden–Fletcher–Goldfarb–Shanno (BFGS) minimization algorithm in the reciprocal space.[53] To account for long-range dispersion interactions, Grimme DFT-D3BJ correction parameters were applied.[54] Atomic positions at pressures of 0, 1.19, 2.74, 4.30, and 5.45 GPa were optimized using experimentally-determined lattice parameters at the corresponding pressures.

Conclusions

This study reveals the high-pressure structural and photophysical response of $(PMA)_2PbCl_4$, establishing a coherent structure–property pathway that links anisotropic compression to excitonic reconfiguration. The material remains phase-stable up to 5.45 GPa owing to the rigid Pb–Cl bonded octahedral layer and cooperative inorganic–organic distortions. These distortions suppress free-exciton emission while stabilizing self-trapped excitons, resulting in resilient broadband luminescence with a peak intensity near 4.5 GPa. Mechanical analyses reveal moderate elastic anisotropy and coexistence of auxetic and conventional responses, while photoluminescence results confirm robust excitonic tunability. Collectively, $(PMA)_2PbCl_4$ emerges as a mechanically robust, pressure-tunable broadband emitter and provides a possibility for exploiting anisotropy and lattice distortions in 2D HOIPs for durable optoelectronic applications.

Author contributions

Muhammad Azeem: writing – original draft, conceptualization, methodology, formal analysis, and data curation. Jinhyuk Choi: review and editing, formal analysis, and data curation. Yeonhak

Jung: formal analysis and data curation. Yongjae Lee: writing – review and editing, funding acquisition, supervision, and methodology and conceptualization. The manuscript was written through contributions from all authors. All authors have given approval to the final version of the manuscript.

Conflicts of interest

There are no conflicts to declare.

Data availability

The data supporting this article have been included as part of the supplementary information (SI). Supplementary information: pressure-dependent organic layers and inorganic sheet thickness, organic cation size and penetration, and single layer thickness at various pressures viewed along the *b* direction (Fig. S1). Le-bail refinements under ambient conditions (Fig. S2). Fitting of lattice parameters by third-order BM-EOS in EosFit7-GUI (Fig. S3). Compressibility indicatrix (Fig. S4). Systematic evolution of bond lengths, bond angles, interatomic distances, and in-plane and out-of-plane distortion under hydrostatic compression (Fig. S5–S11). Changes in Pb–Pb, Cl–Cl, Pb–N, and C–C/N under pressure (Fig. S12). 3D counterplot of the slowness surface (Fig. S13). Anisotropic distribution of Young's modulus, shear modulus, and Poisson's ratio in 2D contour form along [100], [010], and [001] (Fig. S14). 2D maps along three directions for sound wave velocity and slow (Fig. S15). PL spectrum collected under ambient pressure after releasing (Fig. S16). Chromaticity and emission characteristics (Fig. S17). Refined lattice parameters obtained at different pressures (Table S1). Variation of bond lengths, bond angles, and interatomic distances under compression from ambient to 4.30 GPa (Table S2). Calculated elastic stiffness tensors from first-principles DFT (Table S3). See DOI: **https://doi.org/10.1039/d5qm00719d**.

Acknowledgements

This work was supported by the Leader Researcher program (NRF-2018R1A3B1052042) of the Korean Ministry of Science and ICT (MSIT). Synchrotron experiments were conducted at the beamline 5A at PLS-II.

References

1 M. E. Kamminga, H.-H. Fang, M. R. Filip, F. Giustino, J. Baas, G. R. Blake, M. A. Loi and T. T. M. Palstra, Confinement Effects in Low-Dimensional Lead Iodide Perovskite Hybrids, *Chem. Mater.*, 2016, **28**, 4554–4562.
2 X. Qi, Y. Zhang, Q. Ou, S. T. Ha, C. W. Qiu, H. Zhang, Y. B. Cheng, Q. Xiong and Q. Bao, Photonics and Optoelectronics of 2D Metal-Halide Perovskites, *Small*, 2018, **14**, e1800682.
3 M. Azeem, Y. Qin, Z.-G. Li and W. Li, Cooperative B-Site Octahedral Tilting, Distortion and A-Site Conformational Change Induced Phase Transitions of a 2D Lead Halide Perovskite, *Mater. Chem. Front.*, 2021, **5**, 7587–7594.
4 L.-C. An, Z.-Y. Li, M. Azeem, W. Li, Y. Qin, F.-F. Gao, S.-D. Han, G.-M. Wang and X.-H. Bu, Near-Full-Spectrum Emission Realized in a Single Lead Halide Perovskite across the Visible-Light Region, *Angew. Chem., Int. Ed.*, 2024, **63**, e202411298.
5 B. Saparov and D. B. Mitzi, Organic–Inorganic Perovskites: Structural Versatility for Functional Materials Design, *Chem. Rev.*, 2016, **116**, 4558–4596.
6 W. Li, Z. Wang, F. Deschler, S. Gao, R. H. Friend and A. K. Cheetham, Chemically Diverse and Multifunctional Hybrid Organic–Inorganic Perovskites, *Nat. Rev. Mater.*, 2017, **2**, 16099.
7 W.-Q. Liao, Y. Zhang, C.-L. Hu, J.-G. Mao, H.-Y. Ye, P.-F. Li, S. D. Huang and R. G. Xiong, A Lead-Halide Perovskite Molecular Ferroelectric Semiconductor, *Nat. Commun.*, 2015, **6**, 7338.
8 K.-Z. Du, Q. Tu, X. Zhang, Q. Han, J. Liu, S. Zauscher and D. B. Mitzi, Two-Dimensional Lead(II) Halide-Based Hybrid Perovskites Templated by Acene Alkylamines: Crystal Structures, Optical Properties, and Piezoelectricity, *Inorg. Chem.*, 2017, **56**, 9291–9302.
9 Z. Liu, Z. Zhang, Y. Liu, R. Luo, Y. Cheng, Y. Shen, K. Wang and M. Wang, Boosting Carrier Mobility in 2D Layered Perovskites for High-Performance UV Photodetector, *Small Methods*, 2025, **9**, e2400887.
10 I. Neogi, A. Bruno, D. Bahulayan, T. W. Goh, B. Ghosh, R. Ganguly, D. Cortecchia, T. C. Sum, C. Soci and N. Mathews, Broadband-Emitting 2D Hybrid Organic–Inorganic Perovskite Based on Cyclohexane-bis(methylamonium) Cation, *ChemSusChem*, 2017, **10**, 3765–3772.
11 S. Chowdhury, M. K. Mukhopadhyay, M. K. Sanyal, S. Bhunia, B. Satpati, R. P. Giri, B. Bharatiya, C. Shen and B. M. Murphy, Solution Processed Hybrid Lead Perovskite Films for White Light Emission and Lasing Applications, *Adv. Funct. Mater.*, 2024, **34**, 2401334.
12 Z.-G. Yu, Optical Deformation Potential and Self-trapped Excitons in 2D Hybrid Perovskites, *Phys. Chem. Chem. Phys.*, 2019, **21**, 22293–22301.
13 Q. Li, F. Ma, X. Peng, T. Gao, B. Xu, L. Huang, J. Bai, Q. Li and W. Zhao, Dynamic Color-tunable Luminescence in Lead-free Perovskites by Asymmetric Energy Transfer and Excitation-Dependent Dual Self-trapped Excitons Emission, *Chem. Eng. J.*, 2025, **521**, 166819.
14 Z. Lin, Y.-N. Wu, S.-Y. Xu, B.-C. Chen, P.-W. Huang, X.-H. Qi, Y.-P. Lin and K.-Z. Du, Dopant Effect on the Optical and Thermal Properties of the 2D Organic–inorganic Hybrid Perovskite $(HDA)_2PbBr_4$, *Dalton Trans.*, 2024, **53**, 1691–1697.
15 Z. Wang, C. Q. Li, J. T. Mo and M. Pan, Simultaneous Achieving Color-tuning Long Persistent Luminescence and Phosphorescent Quantum Yield of 81.05% in 2D Organic Metal Halide Perovskite, *Aggregate*, 2025, **6**, e696.
16 A. Jaffe, Y. Lin and H. I. Karunadasa, Halide Perovskites under Pressure: Accessing New Properties Through Lattice Compression, *ACS Energy Lett.*, 2017, **2**, 1549–1555.

17 X.-Z. Zhao, F.-F. Gao, W. Li, Z.-G. Li, Y. Zhang, K. Li, H. Hu, W. Cai, J. Zhang and X.-H. Bu, Pressure Enables High-standard White Light Emission and Significant Emission Enhancement in a 2D Halide Perovskite, *J. Mater. Chem. C*, 2024, **12**, 4599–4605.
18 L. Zhang, L. Wu, K. Wang and B. Zou, Pressure-Induced Broadband Emission of 2D Organic–Inorganic Hybrid Perovskite (C6H5C2H4NH3)2PbBr4, *Adv. Sci.*, 2019, **6**, 1801628.
19 H.-Q. Gao, W. Wei, L.-S. Li, Y.-H. Tan and Y.-Z. Tang, Mechanical Properties of a 2D Lead-Halide Perovskite, (C6H5CH2NH3)2PbCl4, by Nanoindentation and First-Principles Calculations, *J. Phys. Chem. C*, 2020, **124**, 19204–19211.
20 G. Feng, Y. Qin, C. Ran, L. Ji, L. Dong and W. Li, Structural Evolution and Photoluminescence Properties of a 2D Hybrid Perovskite under Pressure, *APL Mater.*, 2018, **6**, 114201.
21 A. Le Bail, Whole powder pattern decomposition methods and applications: A retrospection, *Powder Diffr.*, 2005, **20**, 316–326.
22 F. Birch, Finite Elastic Strain of Cubic Crystals, *Phys. Rev.*, 1947, **71**, 809–824.
23 J. González-Platas, M. Alvaro, F. Nestola and R. Angel, EosFit7-GUI: A New GUI for Equations of State and Strain Analyses and Teaching, *J. Appl. Cryst.*, 2016, **49**, 1377–1382.
24 M. J. Cliffe and A. L. Goodwin, PASCal: A Principal Axis Strain Calculator for Thermal Expansion and Compressibility Determination, *J. Appl. Cryst.*, 2012, **45**, 1321–1329.
25 M. G. Basavarajappa, M. K. Nazeeruddin and S. Chakraborty, Evolution of Hybrid Organic–inorganic Perovskite Materials Under External Pressure, *Appl. Phys. Rev.*, 2021, **8**, 041309.
26 M. Azeem, J. Choi, Y. Jung and Y. Lee, Pressure-Driven Structural and Optoelectronic Tuning of Cl Substituted 2D Lead Halide Perovskite $(ClPMA)_2PbI_4$, *J. Phys. Chem. Lett.*, 2025, **16**, 9791–9799.
27 A. Maufort, M. Van Landeghem, M. Deutsch, P. Banks, P. La Magna, K. Van Hecke, J. Cerdá, L. Lutsen, D. Vanderzande and C. Quarti, Structural Rigidity, Thermochromism and Piezochromism of Layered Hybrid Perovskites Containing an Interdigitated Organic Bilayer, *Chem. Sci.*, 2025, **16**, 5662–5675.
28 S. B. Saadatmand, S. Shokouhi, V. Ahmadi and S. M. Hamidi, Metastructure Engineering with Ruddlesden–Popper 2D Perovskites: Stability, Flexibility, and Quality Factor Trade-Offs, *ACS Omega*, 2024, **9**, 24925–24932.
29 Y. Gupta, S. Rathore, A. Singh and A. Kumar, Tailoring the Mechanical Response of Ruddlesden-Popper Lead Halide Perovskites, *J. Alloys Compd.*, 2022, **901**, 163575.
30 S. Rathore, G. Han, A. Kumar, W. L. Leong and A. Singh, Elastic Modulus Tailoring in $CH_3NH_3PbI_3$ Perovskite System by the Introduction of Two Dimensionality Using $(5\text{-}AVA)_2PbI_4$, *Sol. Energy*, 2021, **224**, 27–34.
31 F. Mouhat and F.-X. Coudert, Necessary and Sufficient Elastic Stability Conditions in Various Crystal Systems, *Phys. Rev. B: Condens. Matter Mater. Phys.*, 2014, **90**, 224104.
32 G. N. Greaves, A. L. Greer, R. S. Lakes and T. Rouxel, Poisson's Ratio and Modern Materials, *Nat. Mater.*, 2011, **10**, 823–832.
33 Z. A. Lethbridge, R. I. Walton, A. S. Marmier, C. W. Smith and K. E. Evans, Elastic Anisotropy and Extreme Poisson's Ratios in Single-Crystals, *Acta Mater.*, 2010, **58**, 6444–6451.
34 X. Liu, P. Yang, Y. Yuan and J. Qu, Sandwich Structure with Negative Poisson's Ratio of Periodic Rectangular Tube: Mechanical Properties and Energy Absorption, *J. Sandwich Struct. Mater.*, 2022, **24**, 2065–2082.
35 C. A. Dalton and E. Göran, Constraints on Global Maps of Phase Velocity from Surface-Wave Amplitudes, *Geophys. J. Int.*, 2006, **167**, 820–826.
36 I. Malashin, V. Tynchenko, D. Martysyuk, N. Shchipakov, N. Krysko, M. Degtyarev, V. Nelyub, A. Gantimurov, A. Borodulin and A. Galinovsky, Assessment of Anisotropic Acoustic Properties in Additively Manufactured Materials: Experimental, Computational, and Deep Learning Approaches, *Sensors*, 2024, **24**, s24144488.
37 H. Liu, T. Wang, C. Wang, D. Liu and J. Luo, Exciton Radiative Recombination Dynamics and Nonradiative Energy Transfer in Two-dimensional Transition-metal Dichalcogenides, *J. Phys. Chem. C*, 2019, **123**, 10087–10093.
38 L. Fu, Y. Wu, C. Zhang, T. Fu and C. Shi, Determination of Radiative and Multiphonon Non-radiative Relaxation Rates of Upconversion Materials, *Phys. Chem. Chem. Phys.*, 2022, **24**, 9953–9963.
39 W. B. Holzapfel, Refinement of the Ruby Luminescence Pressure Scale, *J. Appl. Phys.*, 2003, **93**, 1813–1818.
40 Y. Zhang, L. Zhu, Z. Yang, W. Tao, Z. Chen, T. Li, H. Lei, C. Li, L. Wang and W. Tian, Transient Photoinduced Pb^{2+} Disproportionation for Exciton Self-trapping and Broadband Emission in Low-dimensional Lead Halide Perovskites, *J. Am. Chem. Soc.*, 2024, **146**, 7831–7838.
41 S. Dai and X. Zhan, Nonfullerene Acceptors for Semitransparent Organic Solar Cells, *Adv. Energy Mater.*, 2018, **8**, 1800002.
42 P. Moraitis, G. van Leeuwen and W. van Sark, Visual Appearance of Nanocrystal-based Luminescent Solar Concentrators, *Materials*, 2019, **12**, 885.
43 H.-Q. Gao, W. Wei, L.-S. Li, Y.-H. Tan and Y.-Z. Tang, Mechanical Properties of a 2D Lead-halide Perovskite (C6H5CH2NH3)2PbCl4, by Nanoindentation and First-principles Calculations, *J. Phys. Chem. C*, 2020, **124**, 19204–19211.
44 A. Hammersley, *ESRF Data Collection and Reduction Methods, Tech. Rep.*, ESRF, Grenoble, France, 1993.
45 J. Choi, T. Vogt and Y. Lee, Structuration of Water in Microporous CAU-10-H under Gigapascal Pressure, *J. Phys. Chem. Lett.*, 2022, **13**, 10767–10770.
46 M. Azeem, M. Asif, D. Gui, L. Dong, C. Pei, P. Lu and W. Li, Elastic and Hydrostatic Behaviour of a Zinc Dietary Supplement, Zinc Glycinate Hydrate, *RSC Adv.*, 2019, **9**, 13153–13158.
47 M. Azeem, K. Li, Y. Qin, L. Dong and W. Li, Mechanical Study of a Copper Dietary Supplement, Copper Glycinate Hydrate, *CrystEngComm*, 2021, **23**, 1815–1820.

48 B. H. Toby and R. B. Von Dreele, GSAS-II: The Genesis of a Modern Open-source All-purpose Crystallography Software Package, *J. Appl. Crystallogr.*, 2013, **46**, 544–549.
49 S. J. Clark, M. D. Segall, C. J. Pickard, P. J. Hasnip, M. I. Probert, K. Refson and M. C. Payne, First principles methods using CASTEP, *Z. Kristallogr. Cryst. Mater.*, 2005, **220**, 567–570.
50 M. C. Payne, M. P. Teter, D. C. Allan, T. A. Arias and J. D. Joannopoulos, Iterative minimization techniques for ab initio total-energy calculations: plane-wave basis sets, *Rev. Mod. Phys.*, 1992, **64**, 1045–1097.
51 J. P. Perdew and A. Zunger, Self-interaction correction to density-functional approximations for many-electron systems, *Phys. Rev. B: Condens. Matter Mater. Phys.*, 1981, **23**, 5048–5079.
52 A. M. Rappe, K. M. Rabe, E. Kaxiras and J. D. Joannopoulos, Optimized pseudopotentials, *Phys. Rev. B: Condens. Matter Mater. Phys.*, 1990, **41**, 1227–1230.
53 H. J. Monkhorst and J. D. Pack, Special points for Brillouin-zone integrations, *Phys. Rev. B: Solid State*, 1976, **13**, 5188–5192.
54 S. Grimme, A. Hansen, J. G. Brandenburg and C. Bannwarth, Dispersion-corrected mean-field electronic structure methods, *Chem. Rev.*, 2016, **116**, 5105–5154.